



Article

Probabilistic Slope Stability Analysis of Mount St. Helens Using Scoops3D and a Hybrid Intelligence Paradigm

Sumit Kumar ¹, Shiva Shankar Choudhary ¹, Avijit Burman ¹, Raushan Kumar Singh ² , Abidhan Bardhan ^{1,*} and Panagiotis G. Asteris ³ 

¹ Department of Civil Engineering, National Institute of Technology, Patna 800005, India; sumitk.phd19.ce@nitp.ac.in (S.K.); shiva@nitp.ac.in (S.S.C.); avijit@nitp.ac.in (A.B.)

² Department of Computer Engineering and Applications, GLA University, Mathura 281406, India; raushan.singh@gla.ac.in

³ Computational Mechanics Laboratory, School of Pedagogical and Technological Education, 14121 Athens, Greece; asteris@aspete.gr

* Correspondence: abidhan@nitp.ac.in

Abstract: In the past, numerous stratovolcanoes worldwide witnessed catastrophic flank collapses. One of the greatest risks associated with stratovolcanoes is a massive rock failure. On 18 May 1980, we witnessed a rock slope failure due to a volcano eruption, and a 2185.60 m high rock slope of Mount St. Helens was collapsed. Thus, from the serviceability perspective, this work presents an effective computational technique to perform probabilistic analyses of Mount St. Helens situated in Washington, USA. Using the first-order second-moment method, probability theory and statistics were employed to map the uncertainties in rock parameters. Initially, Scoops3D was used to perform slope stability analysis followed by probabilistic evaluation using a hybrid computational model of artificial neural network (ANN) and firefly algorithm (FF), i.e., ANN-FF. The performance of the ANN-FF model was examined and compared with that of conventional ANN and other hybrid ANNs built using seven additional meta-heuristic algorithms. In the validation stage, the proposed ANN-FF model was the best-fitted hybrid model with $R^2 = 0.9996$ and $RMSE = 0.0042$. Under seismic and non-seismic situations, the reliability index and the probability of failure were estimated. The suggested method allows for an effective assessment of the failure probability of Mount St. Helens under various earthquake circumstances. The developed MATLAB model is also attached as a supplementary material for future studies.

Keywords: reliability analysis; rock slope stability; Scoops3D; artificial neural network; swarm intelligence

MSC: 68T09; 68T20



Citation: Kumar, S.; Choudhary, S.S.; Burman, A.; Singh, R.K.; Bardhan, A.; Asteris, P.G. Probabilistic Slope Stability Analysis of Mount St. Helens Using Scoops3D and a Hybrid Intelligence Paradigm. *Mathematics* **2023**, *11*, 3809. <https://doi.org/10.3390/math11183809>

Academic Editor: Zongwei Luo

Received: 8 August 2023

Revised: 30 August 2023

Accepted: 31 August 2023

Published: 5 September 2023



Copyright: © 2023 by the authors. Licensee MDPI, Basel, Switzerland. This article is an open access article distributed under the terms and conditions of the Creative Commons Attribution (CC BY) license (<https://creativecommons.org/licenses/by/4.0/>).

1. Introduction

Volcanic edifices have slope failures that range from small rocks falling to massive collapses. Enormous flank (with volume $> 0.1 \text{ km}^3$) slides have significantly changed over 200 stratovolcanoes across the globe [1] and are among the most sudden, damaging, and potentially hazardous volcanic events. As a result of catastrophic side collapses, many volcanoes and stratovolcanoes have changed in big ways worldwide [2]. The most significant volcanic collapses in history, such as those observed at Bandai (Japan), Mount St. Helens (USA), and Bezymianny (Russia), were initiated by the movement along extensive curved failure surfaces [3]. In the United States, Mount St. Helens had a terrible fall in 1980 [4]. Debris avalanches, which can later mobilize into debris disasters, pose major threats to the structure and areas further downslope or downstream when these enormous collapses occur, often involving more than 0.1 km^3 of material. Moreover, a significant number of approximately 700 stratovolcanoes found on Earth present a potential hazard to individuals

residing in developing nations. As a result, methods for rapid and cost-effective hazard evaluations are particularly important. In the past, approximately 20,000 individuals have lost their lives by flank collapses [5]. There exist numerous processes that can lead to the instability of edifices [3]. The collapse of such structures can be attributed to volcano-specific factors such as magma intrusion, hydrothermal alteration, and thermal pressurization of pore fluids [6]. Alternatively, it can be caused by more universally recognized factors associated with slope instability, such as increased pore fluid pressures. Mount St. Helens has experienced multiple flank collapses, making it an ideal site for a comprehensive assessment of its stability.

In the past, slope stability assessments have been performed in two dimensions, with the assumption that plane strain conditions are true. Since the 1930s, there has been a lot of interest in slope stability studies [7]. However, it is important to mention that a three-dimensional (3D) slope assessment procedure would generate accurate results [8]. This is especially the case when the geometry of the slopes varies widely. In addition, two-dimensional (2D) plane strain assumptions become invalid near the corners of a finite slope [9]. For simple hillslope shapes, 2D slope stability assessments typically produce lower factor of safety (FOS) values than 3D approaches; however, the variations between these two approaches are often in the range of 10% to 20% [10,11]. In the recent past, researchers have investigated 3D slope stability [8,12,13]. Hungr [14] proposed a method for estimating the FOS of 3D slopes using the 2D Bishop's approach [15]. Based on the general limit equilibrium method and as per the work of Lam and Fredlund [16], Fredlund and Krahn [17] also proposed a 3D approach. However, several techniques have been devised for analyzing slope stability. The limit analysis method [18], the limit equilibrium method (LEM) [19], and the strength reduction method (SRM) [18] are the common approaches. Among these methods, the LEM and SRM are deterministic because they use predetermined values for individual soil properties to infer the stability of a slope.

Despite providing a conservative analysis, FOS-based approaches have been stated to be ineffective in several cases [20]. The deterministic approach has a significant drawback when accounting for uncertainties in soil parameters. Specifically, parameters such as cohesion (c), angle of internal friction (ϕ), bulk density (γ), and external loads are not explicitly considered in the FOS approaches [20]. Furthermore, the determined value of the FOS is frequently employed for a specific objective, such as assessing the long-term stability of slopes, irrespective of the uncertainty associated with the estimation. However, it is not practical to apply the same FOS to several scenarios with varying uncertainty levels. Notably, soil materials are highly complex because of their non-linear stress-strain correlations, elastoplastic behavior under different loading conditions, and time-dependent stress-strain responses [21]. Thus, it is imperative to conduct a thorough investigation of geotechnical parameters to consider the inherent uncertainties associated with soils during slope stability assessments, and reliability analysis (RA) is considered to be deemed appropriate in such circumstances [22].

Using probability theory and statistics, uncertainties in soil parameters are rationally comprised of geotechnical analyses [23]. Reliability index (β) and probability of failure (POF) are commonly employed measures for assessing the performance of geotechnical designs. The probability of not meeting performance standards is known as the POF [23]. RA of geotechnical structures can be performed using a variety of methodologies, including direct first-order second-moment method (FOSM) [23], first-order reliability method (FORM) [24], and Monte Carlo simulation (MCS) method [25]. The aforementioned techniques employ probabilistic assessments of soil characteristics and sub-soil stratigraphy as input variables and yield the output β and/or POF for a pre-established structures [23]. Nevertheless, limited attention has been given to the application of these techniques in the context of mitigating mountain slope instability.

Previous approaches have also addressed the use of implicit performance functions. The response surface method (RSM) is one of them [26]. The implicit performance functions are approximated by RSM using a polynomial function. A fairly precise approximation

of β can be generated if the selected polynomial functions fit the limit state well [27]. In contrast, several machine learning (ML) techniques have previously been employed for slope stability analysis in soil, including multivariate adaptive regression splines (MARS), relevance vector machine (RVM), artificial neural network (ANN), support vector machine (SVM), extreme learning machine (ELM), and various others [28]. ML algorithms are capable of efficiently simulating slope reliability difficulties by approximating implicit performance functions [22,23].

Numerous ML methods, such as ANN, MARS, RVM, and ELM, have previously been employed to tackle various engineering issues [28], including RA of different soil slopes [22]. Radial basis function networks and ANNs were utilized by Deng [29] and Deng et al. [30], respectively, for structural RA. Cho [31] used RSM based on ANN to carry out probabilistic slope analyses. Erzin and Cetin [32] used ANN to calculate the FOS of a soil slope. Several researchers have also examined slope reliability analysis using RVM, SVM, MARS, and other ML approaches [23]. Kang et al. [33] employed replacement models with updated SVMs and two swarm intelligence methods, viz., particle swarm optimization (PSO) and artificial bee colony (ABC) algorithms. Zhao [20] used SVM for slope RA. RA of soil slopes using RVM-based RSM, multi-kernel RVM, and enhanced FOSM were also performed [34].

Nonetheless, it should be noted that earthquakes can trigger a considerable number of earth and rockslides, leading to an extensive destruction of prominent structures such as hills, hill-highways, railway tracks, dam reservoirs, etc. Note that, the stability of a slope is significantly influenced by the geometry of its shape and the physical properties of the existing soils. Slope failures can cause ground deformation, which in turn can damage structures. Instability is a common problem in hilly areas because of their geodynamic and structural makeup and the effects of factors like extreme rainfall, urbanization, and other influences [35]. High-quality roads and highways are desperately needed in these mountainous areas to facilitate easier travel, more visitors, and risk-free development efforts. The significance of performing slope stability analyses that consider the spatial variability of geotechnical characteristics inside a prominent volcanic formation like Mount St. Helen is of utmost relevance.

Furthermore, existing literature exhibits no prior utilization of high-performance ML approaches for probabilistic evaluations of Mount St. Helens in seismic and non-seismic conditions. Thus, considering the above points, probabilistic assessments of Mount St. Helens were carried out in this study using a hybrid intelligence approach of ANN and a meta-heuristic approach. For this purpose, the details of slope geometries provided by Reid et al. [36] were used for modeling spherical failure surfaces using the 3D Bishop approach. For estimating FOS, Scoops3D, an open-source platform, was used, followed by probabilistic assessments in seismic and non-seismic conditions.

2. Research Significance

Numerous studies have emphasized the use of ANNs in the domains of engineering and science [28]. The ability of ANNs to represent non-linear problems without considering a functional relationship between input and output is a significant advantage over other ML algorithms. Furthermore, the output generation is unaffected by one or more corrupted cells. Despite these advantages, ANN possesses notable limitations, including challenges related to the entrapment in local minima and the occurrence of overfitting. Moreover, the challenge of accurately determining the precise global minimum can lead to unfavorable outcomes [28]. To address these issues, researchers employed various optimization algorithms (OAs), including PSO, ABC, and genetic algorithm (GA) [28]. Due to their robust global search capabilities, OAs can iteratively optimize the learning parameters of ANNs, resulting in enhanced prediction performance. Over the past decade, there has been a significant increase in the utilization of hybrid ANNs, such as ANN-ABC, ANN-GA, ANN-PSO, etc., for addressing various problems [28,37]. Tun et al. [38] used GA to assess 3D slopes with several failure regions. Nevertheless, it should be noted that there is a lack

of research on the reliability of slope analysis for the Mount St. Helens utilizing hybrid ANNs. Moreover, no study has been conducted on the evaluation of hybrid ANNs that are built using different groups of OAs for slope stability analysis in cone-shaped terrains.

Thus, this study aims to address the gap in the literature by using hybrid ANNs built with different groups of OAs to perform a probabilistic analysis of Mount St. Helens. Specifically, eight distinct OAs viz., ALO, BBO, CPA, DE, EO, FF, GA, and PSO (see Section 5.2 for details) were used to optimize weights and biases ANNs, resulting in eight hybrid ANNs, viz., ANN-ALO, ANN-BBO, ANN-CPA, ANN-DE, ANN-EO, ANN-FF, ANN-GA, and ANN-PSO. The computational findings were used to select the most effective hybrid ANN model for performing RA of Mount St. Helens under seismic and non-seismic conditions. The outcomes of the current study were compared to the findings of Tun et al. [38] and evaluated in the subsequent sections.

3. Study Area

This study investigates RA of Mount St. Helens, located in Skamania County, Washington, USA, approximately 55 km west of Mount Adams in the western part of the Cascade Range, experienced a catastrophic eruption on 18 May 1980 [4]. Notably, the failure surfaces may be readily apparent for basic geometrical aspects of a slope (such as polygonal or polyhedral-shaped slopes), but this may not be the case for more complex/real topographies like Mount St. Helens. Thus, the present study utilizes the details of Mount St. Helens (obtained from Google Earth) to conduct probabilistic slope analyses. The use of Google Maps and Google Earth images has facilitated the depiction of Mount St. Helens' geographical location and topographical features, presented in Figure 1.

Before the tragic collapse of Mount St. Helens, rock strength and density distributions in 3D were unknown. After the collapse, Voight et al. [4] and Glicken [39] used geologic sections provided by Hopson and Melson [40] to recreate the inner geology structure. The mountain's core comprises earlier dacite dome lavas and flank breccias hydrothermally altered. This unit was covered by andesitic, basaltic, and tephra lava flows. Summit and Goat Rocks domes were built with more modern dacite. The dacitic crypto-dome intruded on each of these components in the year 1980.



Figure 1. Location and topographical representations of the study area of Mount St. Helens.

4. Methodology

Theoretical detail of the deterministic analysis to calculate the FOS using Bishop's simplified method is presented in this section, followed by the details of probabilistic analysis to conduct reliability analyses.

4.1. Deterministic Analysis

The FOS of slope failure in 3D was calculated using Scoops3D, a computer software that employs Ordinary and Bishop simplified methods. As stated above, Bishop's simplified method was employed in this study, wherein spherical failure surfaces were utilized to analyses 3D slopes. The simplified form of Bishop's approach for calculating FOS in the absence of groundwater is given:

$$FOS = \frac{\sum R_{j,k}(c_{j,k}A_{j,k} + W_{j,k}\tan\phi_{j,k})/m_{\alpha_{j,k}}}{\sum W_{j,k}[R_{j,k}m_z + k_{eq}e_{j,k}]}; m_{\alpha_{j,k}} = \cos\varepsilon_{j,k} + \tan\phi' dm_z \text{ and } m_z = \sin\alpha_{j,k} \quad (1)$$

where $c_{j,k}$ is the effective cohesion; $\phi_{j,k}$ is the effective internal friction angle; $R_{j,k}$ is the distance from the j, k column's trial slip region to its axis of rotation, $A_{j,k}$ is the column's trial surface area, $W_{j,k}$ is the column's weight; $e_{j,k}$ is the horizontal driving force moment arm. A free-body diagram of the j, k column is shown in Figure 2. Note that, for a 3D formulation, it is also assumed that the combined normal and shear forces acting along the sides of the columns be zero in both the x and y axes.

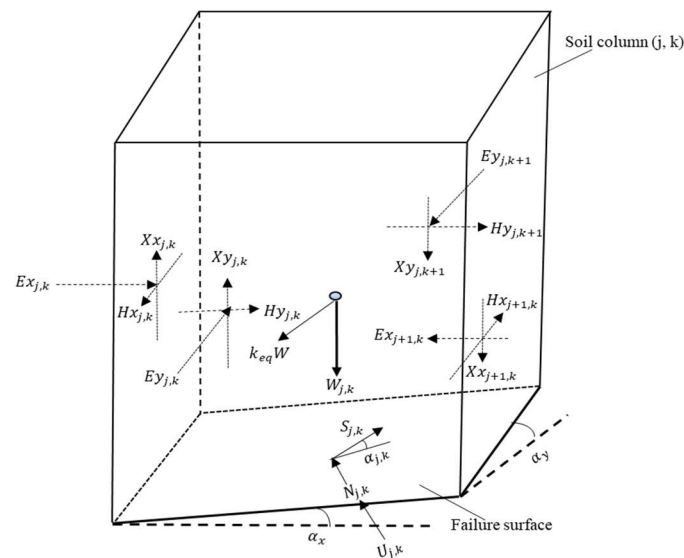


Figure 2. Free body diagram of the j, k column.

In Figure 2, W denotes the column's weight; $E_{xj,k}$ and $E_{yj,k}$ denote inter-column normal forces in x and y axes, respectively; $H_{xj,k}$ and $H_{yj,k}$ are horizontal shear forces in y-z plane; $X_{xj,k}$ and $X_{yj,k}$ denote inter-column shear forces occurring in the x-z plane; $N_{j,k}$ and $U_{j,k}$ denote effective normal force and pore water force at the base, respectively; $S_{j,k}$ denotes mobilized shear force on the base; $\alpha_{j,k}$ denotes x-y plane slide angle, and α_x and α_y denote the base inclination of the middle column in the x-z and y-z planes, respectively.

4.2. Digital Elevation Modelling

A digital representation of the topographic relief is commonly called a digital elevation model (DEM) [41]. Notably, regular grids are the most commonly encountered type of DEMs, and they are offered in various forms [42]. DEM is widely used in geomorphology, representing various landscape features and offering other benefits, including efficient data storage and processing power. The accuracy of a DEM is influenced by various factors pertaining to the topography, such as landforms, elevations, texture, ruggedness,

and vegetation. The accuracy is also influenced by the methods employed for collecting elevation data, the specific process for generating the DEM, the type of grid employed for the DEM, and the resolution of the DEM [43]. Also, the LiDAR-DEM (light detection and ranging-DEM) to the DEM was created using 1×1 m horizontal resolution and 0.2 m vertical precision from data collected using airborne laser scanning (ALS) [44–48]. In addition, remote sensing allows for massive mountain ranges, deep valleys, and ocean floor magnetic striping [49].

The United States Geological Survey (USGS) developed a free software package, Scoops3D, to analyze the 3D stability of slopes based on DEM [36]. To begin with, precise calculations of the terrain's topography are required. As a result, because DEM can easily employ spatial and picture data from geographic information systems (GIS), it may be used to develop a 3D model for slope concerns [50]. In the context of probabilistic analyses, it is adequate to consider the variations in material properties along with the slope geometry. Also, with the increasing use of satellite images and aerial photography, DEM representations are more accessible than ever. Reid et al. [36] used 100-m resampled DEMs to accurately compute the stability of potential failures with a volume $> 0.1 \text{ km}^3$. However, the DEM provided by Reid et al. [36] was used in this study, generated from photographs taken on 12 May 1980 (see Figure 3). Additionally, Figure 4 depicts the DEM profile of Mount St. Helens and necessary information was extracted from the work of Reid et al. [36] for this study.



Figure 3. Aerial view of Mount St Helens before its 1980 eruption.

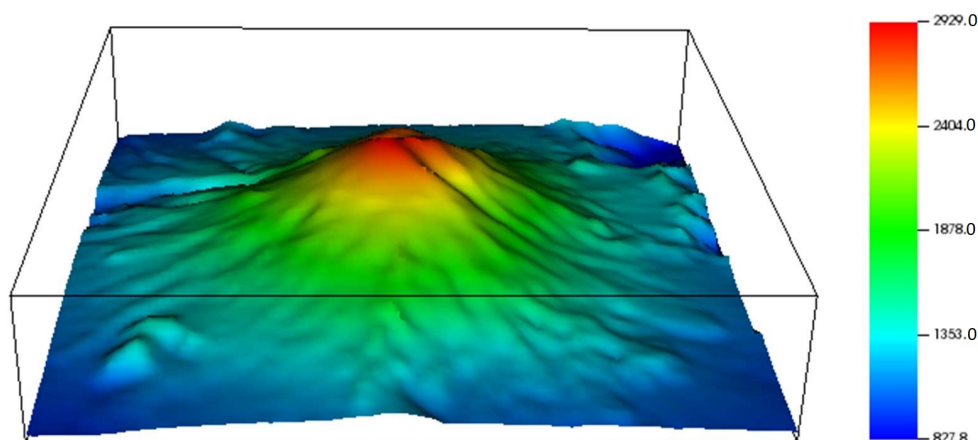


Figure 4. DEM illustration of Mount St. Helens.

4.3. Probabilistic Analysis

Inaccuracies in modelling, subsurface stratigraphic uncertainty, and intrinsic spatial variability of soil and rock characteristics are some of the uncertainties that can affect a slope stability analysis. Using probability theory and statistics, the intrinsic spatial variability of soils and rocks and other soil and rock characteristics uncertainties can be considered in geotechnical analysis and/or design. This gives a balanced way to avoid these uncertainties in the analysis of slope stability study [23,24]. The reliability of a slope is explained as the probability that the performance standards will not be met. In other terms, the POF is the probability that the minimum FOS is less than one, i.e., $POF = P(FOS < 1)$.

Assume that $g(x)$ is a performance function used to determine the FOS, and that $g(x)$ has a series of random variables $x = [x_1, x_2, x_3, \dots, x_k]$ denoting uncertain model parameters. Thus, the value of β is given by:

$$\beta = \frac{\mu_{FOS} - 1}{\sigma_{FOS}} \quad (2)$$

where μ_{FOS} and σ_{FOS} denote the mean and standard deviation of the FOS, respectively. The μ_{FOS} signify the value of $g(x)$ at mean values of $\mu_1, \mu_2, \dots, \mu_K$ random variables $x_1, x_2, x_3, \dots, x_k$, given by:

$$\mu_{FOS} = g(\mu_1, \mu_2, \dots, \mu_K) \quad (3)$$

The σ_{FOS} is defined as:

$$\sigma_{FOS} = \sqrt{\sum_{i=1}^k \sigma_i^2 \left(\frac{\partial g}{\partial x_i} \right)^2 + \sum_{i=1}^k \sum_{j \neq 1}^k \rho_{i,j} \sigma_i \sigma_j \frac{\partial g}{\partial x_i} \frac{\partial g}{\partial x_j}} \quad (4)$$

where σ_i denotes the random variable's standard deviations x_i ; $\rho_{i,j}$ denotes the correlation coefficient between the two distinct unknowable variables, x_i and x_j ; $\frac{\partial g}{\partial x_j}$ are the performance function's partial derivatives with respect to x_i . Hence, the P_f of slope can be obtained using $POF = 1 - \Phi(z)$, where Φ represents cumulative standard distribution function with $\mu = 0$ and $\sigma = 1$.

5. Overview of Employed Models

This section provides a comprehensive overview of the computational models utilized in the present study. Firstly, a concise introduction to ANN, followed by a brief overview of meta-heuristic algorithms. Following this, the methodology for constructing a hybrid ANN is described and explained

5.1. Artificial Neural Network

ANNs are a subset of ML models that are constructed based on the principles of neuronal organization observed in biological neural networks found in animal brains. ANNs acquire information from the given dataset and produce predictions in response. ANN consists of one input layer, one or more hidden layers, and one output layer (see Figure 5). Neurons that are not computational collect information in the input layer, whereas computational neurons execute linear/non-linear computations in the hidden and output layers. Notably, weighted connections connect each and every neuron in the input, hidden, and output layers. The hidden and output layers both have biases that are proportional to the number of respective neurons. Input and output layers have a relationship between their respective numbers of input and output variables and their number of neurons. The number of hidden neurons varies from problem to problem and is selected through trial and error.

In ANN, weights and biases are calculated iteratively to reduce the discrepancy between estimated and real values. The fitness function most frequently employed is the root mean square error (RMSE) index. Multiple training techniques, including conjugate gradient, gradient descent, Levenberg-Marquardt functions, etc., are used during the training of ANN and to adjust weights and biases. Application of ANNs in different engineering domains can be seen in the literature [51–55].

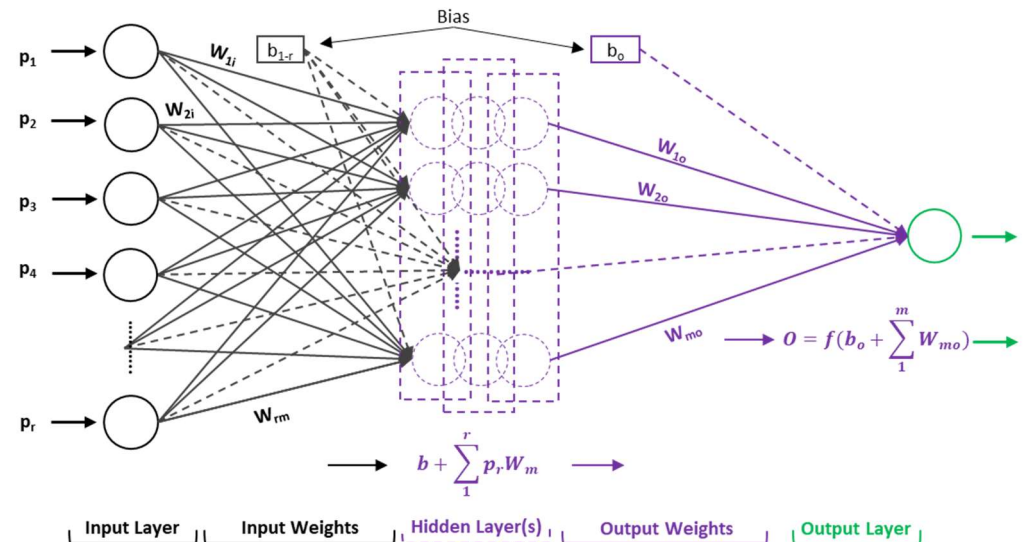


Figure 5. Architecture of ANNs.

5.2. Overview of OAs

The complexity and difficulty of solving challenges in the actual world have increased during the past few decades. As a result, optimization techniques, especially meta-heuristic algorithms, have become important. These techniques, which approximate optimal solutions, rely on randomness. The optimization strategy determines the optimal decision variables through minimizing or maximizing the objective function. Due to their simplicity and ease of implementations, meta-heuristic algorithms have been deployed as an alternative solution. OAs are categorized into two main groups: (a) pop-based, which considers the entire population, and (b) single-solution-based, which considers only one possible solution [56]. Notably, most of the pop-based OAs have been derived from natural phenomena. Figure 6 presents a classification of different kinds of pop-based OAs.

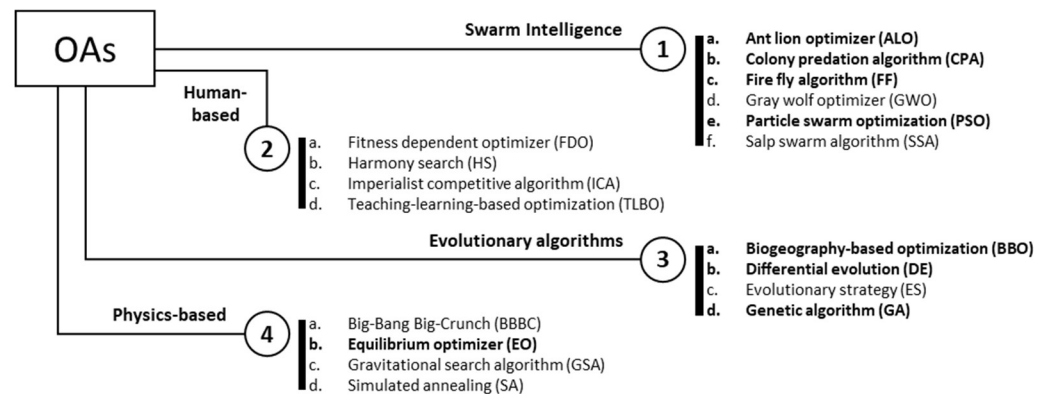


Figure 6. Classification of meta-heuristic OAs.

The categorization of pop-based OAs can be based on their sources of inspiration, which include algorithms inspired by swarm intelligence (SI), algorithms based on human behavior, algorithms derived from evolutionary algorithms (EAs), and physics-based algorithms. SI algorithms replicate the social behaviors of organisms residing in swarms, flocks, and herds. The class of SI algorithms includes various approaches such as ALO [57], CPA [58], FF [59], GWO [60], PSO [61], and SSA [62], among others. The second group of OA pertains to human-based algorithms derived from the collective behavior and collaborative problem-solving approaches exhibited by individuals working in groups. The algorithms encompassed within this category include FDO [63], HS [64], ICA [65], TLBO [66], etc. EAs simulate natural evolutionary processes like mutation, selection, and recombination. BBO [67], DE [68], ES [69], and GA [70] are some of the examples of this group. The final category of popular algorithms draws inspiration from the rules of physics. BBBC [71], EO [72], GSA [73], and SA [74] are some examples of physics-based OAs. As stated above, eight OAs (viz., ALO, BBO, CPA, DE, EO, FF, GA, and PSO) from different groups were considered in this study, which are widely used in different engineering domains. Notably, detailed working principles of these OAs are not presented in this study because they are well established, and the original works of ALO [57], BBO [67], CPA [58], DE [68], EO [72], FF [59], GA [70], and PSO [61] can be referred to for more details.

5.3. Hybridization Procedure of ANN and OAs

Numerous studies have been done in the previous few decades on how to use multiple OAs to enhance the performance of conventional ANNs. The ANN may not perform well in some cases since back-propagation isn't great at locating precise global minima [51,75]. ANNs are susceptible to becoming trapped in local minima, unlike OAs, which can adjust their learning parameters to overcome this obstacle. OAs have the flexibility to perform exploration and exploitation techniques and generate optimal values for ANN weights and biases. The construction process of hybrid ANNs involves the following steps: (a) initialization of ANN; (b) selection of hyper-parameters, i.e., the number of hidden layers (N_{HL}) and the number of hidden neurons (N_H); (c) random generation of weights and biases; (d) initialization of deterministic parameters for the OA, such as population/swarm size (N_S), maximum number of iterations (itr_{max}), upper and lower bounds (ub and lb), etc.; (e) training of ANN using training dataset; (f) evaluation of fitness; (g) generation of learning parameters when termination criteria are met; (h) validation of ANN; and (i) formation of final ANNs with optimized weight and bias values. Figure 7 is a flowchart depicting the aforementioned steps. The given equation can be utilized to compute the overall count of optimized weights and biases, (O_{w+b}), $O_{w+b} = r \times N_H + N_H + N_H + o$, with r and o representing the number of input and output neurons, respectively.

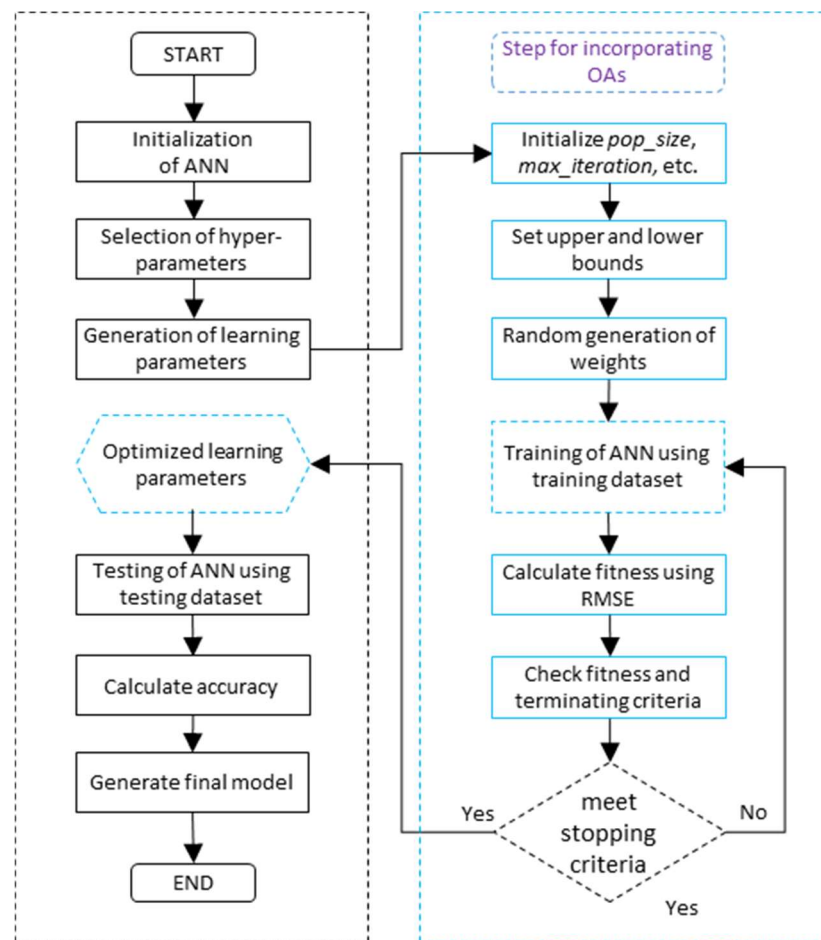


Figure 7. Illustration of construction procedure of hybrid ANNs.

6. Data Description and Modelling

The geology of Mount St. Helens appeared more consistent before it collapsed due to volcanic eruptions than that of surrounding stratovolcanoes. Voight et al. [4] described the physical properties of debris avalanche materials. Intact edifice rock was found to have an average unit weight of 24 kN/m^3 , and average values of ϕ and c were 40° and 1000 kN/m^2 , respectively. This information was used to perform the slope stability analysis. Following the normal distribution sampling technique, a total of 100 samples were generated using mean values of $c = 1000 \text{ kN/m}^2$, $\phi = 40^\circ$; and $\gamma = 24 \text{ kN/m}^3$. Subsequently, the FOS of the slope was determined using Scoops3D for the generated samples with five distinct values of seismic coefficient (k_e), viz., 0 (for non-seismic case), 0.05, 0.10, 0.15, and 0.20, referred to as Set 1 to Set 5, respectively. Descriptive details of the 500 samples (i.e., 100 samples against each k_e value) are presented in Table 1. The present study incorporates certain simplifications, including the assumption of homogenous material properties, intact rock mass, the exclusion of groundwater effects, and the inclusion of seismic loading. However, according to Table 1, the parameter c varies from 809.77 kN/m^2 and 1195.17 kN/m^2 . The ranges for the remaining parameters, ϕ , γ , and k_e are 35.18° to 49.40° , 22.02 kN/m^3 to 25.99 kN/m^3 and 0 to 0.20, respectively. The other descriptive details can be seen in Table 1.

Stage I: After FOS estimations, the primary database of 500 records was finalized. This database was normalized randomly between 0 and 1 and then divided into training and testing subsets. Using 5-fold cross-validation, 80% of the entire dataset was used for training, i.e., 400 samples, whereas the remaining 20%, i.e., 100 samples, were used for testing. Notably, the training subgroup was used to construct hybrid ANNs, while the testing subgroup was used for validation. After model construction, multiple performance matrices, namely mean absolute error (MAE), Nash-Sutcliffe efficiency (NSE), performance

index (PI), coefficient of determination (R^2), RMSE, and weighted mean absolute percentage error (WMAPE), were determined and assessed. Subsequently, the best-forming hybrid ANN was selected for the probabilistic assessment of Mount St. Helens.

Stage II: Subsequent to the selection of the best-performing model, RA was performed in seismic and non-seismic conditions. This was achieved by producing different sets of input parameters with different coefficient of variation (COV) values. The following stage involves the normalization of the new dataset based on the original input variables (see Table 1). The best-obtained paradigm was then used to generate FOS, followed by a probabilistic assessment of the slope. Figure 8 shows the entire process of FOS estimation and probabilistic analyses of Mount St. Helens.

Table 1. Descriptive details of the generated dataset.

Index	c (kN/m ²)	ϕ (°)	γ (kN/m ³)	k_e
Min.	809.77	35.18	22.02	0.00
Mean	1000.00	40.00	24.00	-
Max.	1195.17	49.40	25.99	0.20
Std. Dev.	117.31	4.21	1.17	0.08
Std. Error	11.73	0.04	0.01	0.02
Kurtosis	−1.26	−1.20	−1.25	−1.20
Skewness	−0.08	−0.09	0.16	0.00

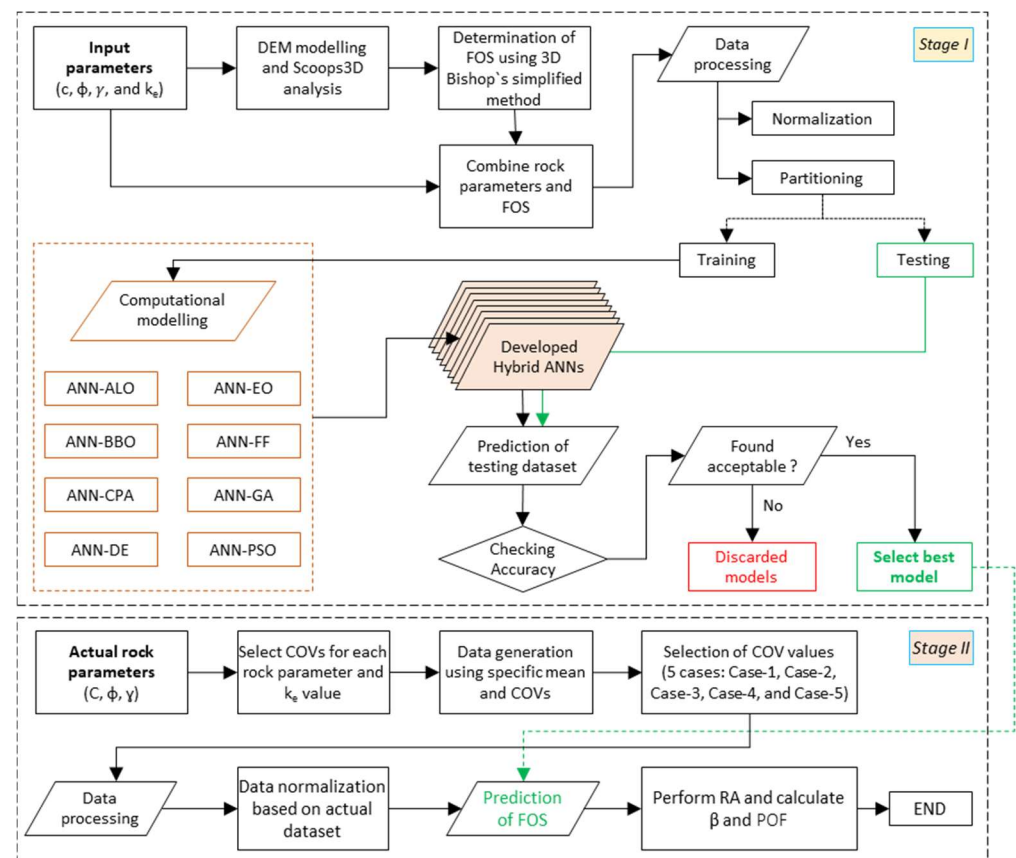


Figure 8. Flowchart depicting the computational modelling.

7. Results and Discussions

This section provides comprehensive assessment of the results obtained from the slope stability analyses, the performance evaluation of hybrid ANNs, and the probabilistic analysis conducted on the slope. However, before presenting the outcomes of probabilistic

assessment, the outcomes of slope stability analysis and parametric configurations of hybrid ANNs are presented and discussed.

7.1. Slope Stability Analysis

As stated above, the slope stability of Mount St. Helen was carried out using the Scoops3D computer program. For each 100 samples, the FOS was computed for five sets of k_e , i.e., Sets 1 to 5. The outcomes of slope stability assessment are demonstrated in Figure 9. Additionally, Figure 10 displays the critical and safest FOS and their related slip circles. Herein, the minimum and maximum FOS obtained in each set (i.e., against each k_e value) are presented against each k_e case. The minimum and maximum values of FOS were determined to be 1.901 and 2.864 for Set 1 (i.e., $k_e = 0$); 1.720 and 2.589 for Set 2 (i.e., $k_e = 0.05$); 1.565 and 2.355 for Set 3 (i.e., $k_e = 0.10$); 1.431 and 2.152 for Set 4 (i.e., $k_e = 0.15$), and 1.311 and 1.975 for Set 5 (i.e., $k_e = 0.20$). After conducting deterministic analyses, the obtained FOS values and rock properties were utilized as input and output variables for probabilistic evaluations of Mount St. Helen. Notably, the generated DEMs of these images are attached via Supplementary Materials.

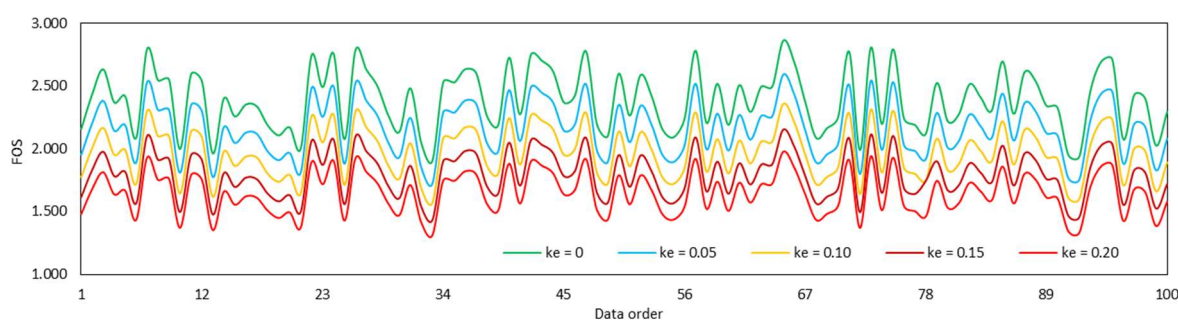


Figure 9. Representation of the Mount St. Helens slope at various k_e values.

7.2. Computational Modelling and Performance Assessment

The derived FOS values were used as the output variable, while the rock parameters viz., c , ϕ , γ , and k_e , were used as the input variables for computational modelling. It is important to note that ANN's hyper-parameters (i.e., N_H and N_{HL}) must be carefully selected to construct the best possible model. Using *Levenberg-Marquardt* backpropagation and *tan-sigmoid* activation functions and RMSE as the fitness function, the most appropriate value of N_H was obtained as 8, i.e., $N_H = 8$ and kept constant for other hybrid ANNs. However, deterministic parameters of OAs, i.e., N_S , itr_{max} , ub , and lb , were also selected using trial-and-error approaches. Since there are four inputs, the total number of O_{w+b} were determined to be 49 (i.e., $4 \times 8 + 8 + 8 + 1$). The values of N_S , itr_{max} , ub , and lb were selected as 50, 500, +1, and -1, respectively. The traditional ANN was also constructed using the above configurations in which RMSE was used as the fitness function.

On the contrary, evaluating the performance of a hybrid model requires examining the convergence behavior of OAs. It exhibits the ability of OAs to conquer local minimum and arrive at a solution more quickly. Convergence curves for all the hybrid ANNs utilized to calculate the FOS are shown in Figure 11. After 500 iterations, the computational cost of the hybrid ANNs were estimated to be 200.72 s, 194.57 s, 437.72 s, 175.03 s, 173.56 s, 4175.92 s, 347.61 s, and 166.87 s, respectively, for ANN-ALO, ANN-BBO, ANN-CPA, ANN-DE, ANN-EO, ANN-FF, ANN-GA, and ANN-PSO. According to Figure 11, the developed ANN-FF achieved faster convergence than other hybrid ANNs constructed for FOS estimation.

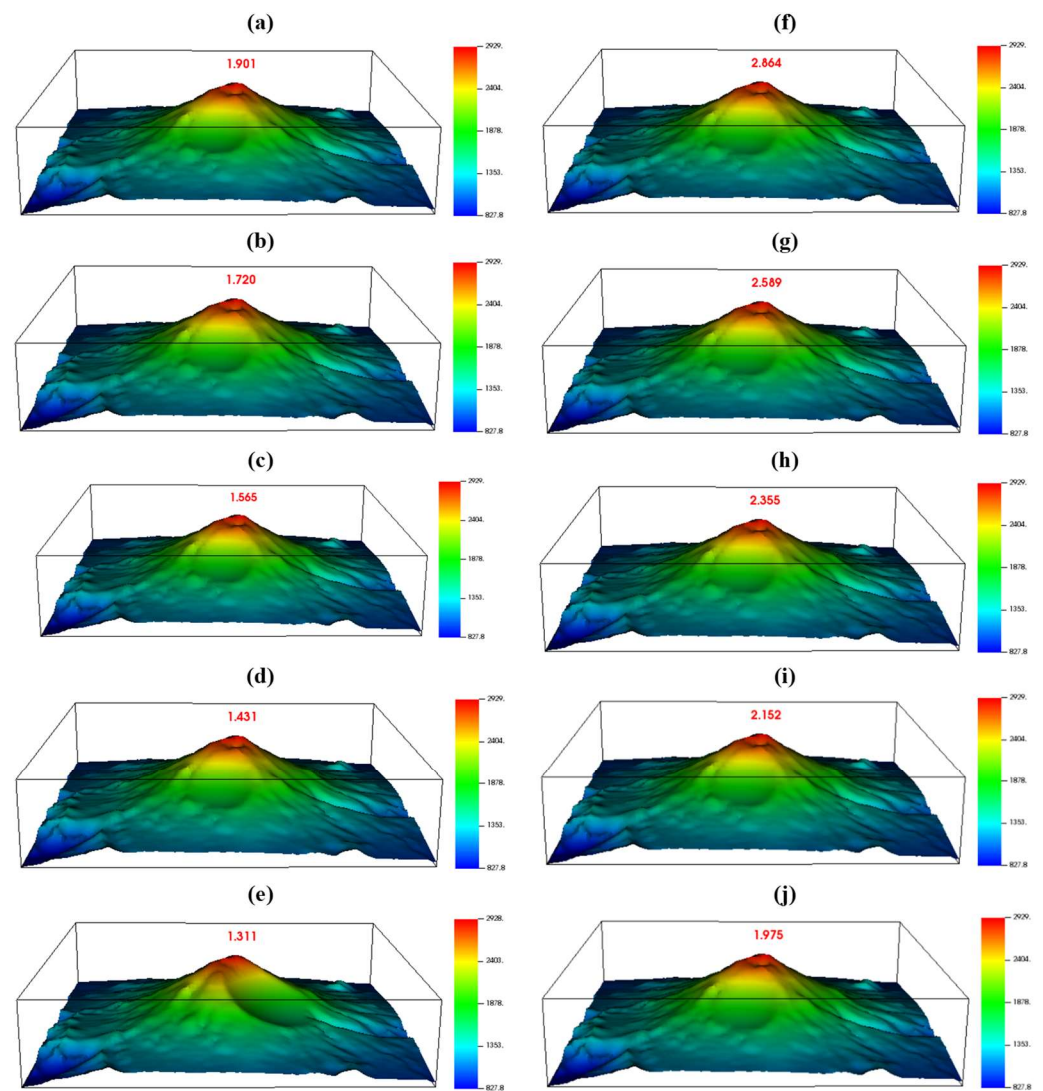


Figure 10. Minimum (a–e) and maximum (f–j) FOS values and corresponding slip circles at different k_0 .

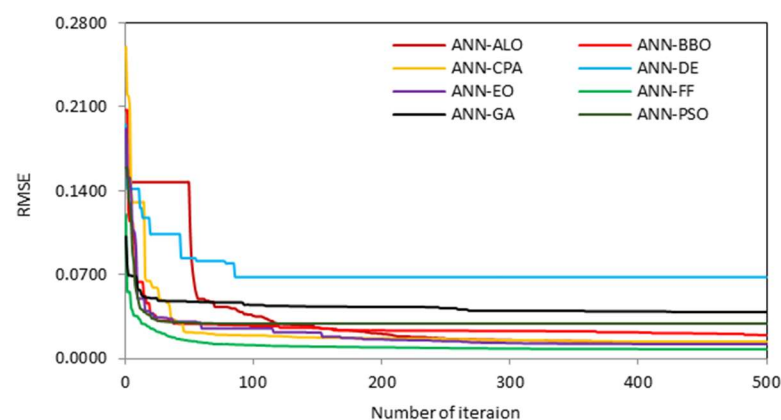


Figure 11. Convergence behaviour of hybrid ANNs.

After model construction, the performance of the developed models was assessed using multiple performance matrices viz., MAE, NSE, PI, R^2 , RMSE, and WMAPE. Among these indices, MAE, RMSE, and WMAPE are the error indices, and NSE, PI, and R^2 are the trend-measuring indices. The use of numerous indices allowed the performance of

the models to be assessed in various ways, including the degree of correlation/fitness, associated error in absolute terms, variance in error, and the amount of variation between the actual and estimated values. Notably, for a perfect prediction model, the value of these indices should be equal to their ideal values as follows: MAE = 0, NS = 1, PI = 2, $R^2 = 1$, RMSE = 0, and WMAPE = 0. These indices are used widely for assessing the performance of data-driven models [28,76,77]. The detailed mathematical expressions of these indices are not presented in this study because they are well-established, and the studies of Bardhan and Samui [28] and Koopialipoor et al. [75] can be referred to for more details.

Tables 2 and 3 display the outcomes of the hybrid ANNs during the training and testing phases, respectively. As stated above, the training subset was used for model construction, while the testing subset was for validation of the constructed models. According to Table 2, the developed ANN-FF realized the desired level of precision ($R^2 = 0.9996$ and RMSE = 0.0041) during the training phase, followed by ANN-EO ($R^2 = 0.9981$ and RMSE = 0.0094), ANN-CPA ($R^2 = 0.9970$ and RMSE = 0.0117), and so on (see Table 2 for other models). Except for ANN-DE, all hybrid ANNs demonstrated a strong fit ($R^2 > 0.95$ or 95%), indicating a strong fit to the FOS database. Also, the employed ANN model exhibits satisfactory performance ($R^2 = 0.9950$ and RMSE = 0.0159). However, among the developed ANNs, the ANN-DE was found to be the least effective model with $R^2 = 0.9039$ and RMSE = 0.0669.

Table 2. Model performance during the training phase.

Indices	ANN-ALO	ANN-BBO	ANN-CPA	ANN-DE	ANN-EO	ANN-FF	ANN-GA	ANN-PSO	ANN
MAE	0.0087	0.0128	0.0088	0.0520	0.0067	0.0031	0.0306	0.0212	0.0124
NS	0.9968	0.9933	0.9970	0.9024	0.9981	0.9996	0.9687	0.9826	0.9949
PI	1.9814	1.9691	1.9824	1.7385	1.9868	1.9952	1.8994	1.9367	1.9738
R^2	0.9968	0.9934	0.9970	0.9039	0.9981	0.9996	0.9688	0.9826	0.9950
RMSE	0.0121	0.0175	0.0117	0.0669	0.0094	0.0041	0.0378	0.0283	0.0159
WMAPE	0.0202	0.0295	0.0204	0.1206	0.0155	0.0072	0.0710	0.0490	0.0266

Table 3. Model performance during the testing phase.

Indices	ANN-ALO	ANN-BBO	ANN-CPA	ANN-DE	ANN-EO	ANN-FF	ANN-GA	ANN-PSO	ANN
MAE	0.0095	0.0144	0.0102	0.0555	0.0078	0.0032	0.0342	0.0255	0.0102
NS	0.9969	0.9927	0.9963	0.8938	0.9978	0.9996	0.9551	0.9722	0.9961
PI	1.9813	1.9667	1.9791	1.7112	1.9853	1.9951	1.8634	1.9074	1.9789
R^2	0.9969	0.9931	0.9964	0.8939	0.9979	0.9996	0.9563	0.9727	0.9961
RMSE	0.0124	0.0188	0.0135	0.0721	0.0103	0.0042	0.0469	0.0369	0.0133
WMAPE	0.0206	0.0311	0.0220	0.1198	0.0169	0.0070	0.0737	0.0549	0.0233

The remaining dataset, referred to as the testing subset, was utilized to assess the model's capacity for generalization after its construction. The performance indicators utilized to evaluate the model's performance during the training phase were also determined for the testing subset and presented in Table 3. The outcomes reveal that the built ANN-FF achieved the highest precision with $R^2 = 0.9996$ and RMSE = 0.0042, followed by ANN-EO ($R^2 = 0.9979$ and RMSE = 0.0103), ANN-ALO ($R^2 = 0.9969$ and RMSE = 0.0124), and so on (see Table 3 for more details). In the testing phase, the performance of the employed ANN was determined to be $R^2 = 0.9961$ and RMSE = 0.0133, which is quite satisfactory compared to some of the hybrid ANNs. Nonetheless, the developed ANN-FF model attained the most precise performance in both phases of FOS estimation. For better demonstration, scatterplot, error plot, and line plot between the actual and estimated FOS values are presented in Figures 12 and 13 for the training and testing phases, respectively. Herein, the best-performing model, i.e., ANN-FF, is only illustrated. In the following sub-section, assessments of the POF of Mount St. Helen are presented.

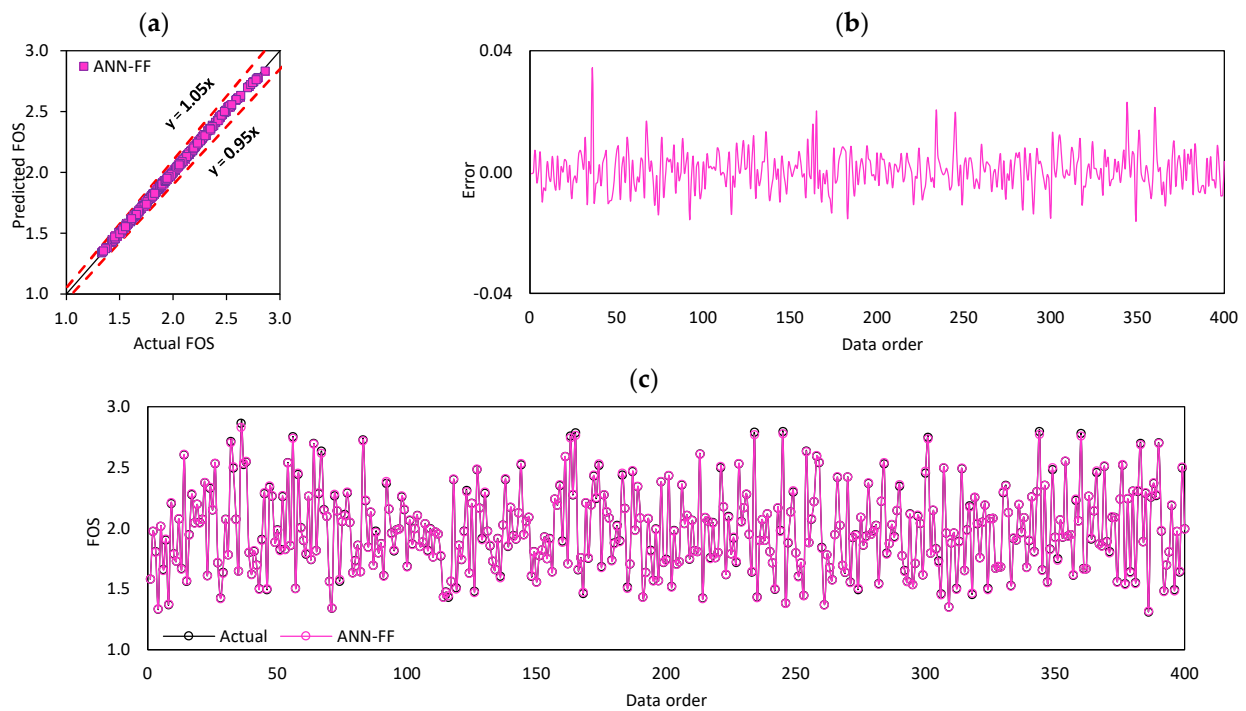


Figure 12. Illustration of (a) scatter plot, (b) error plot, and (c) line plot for the training dataset.

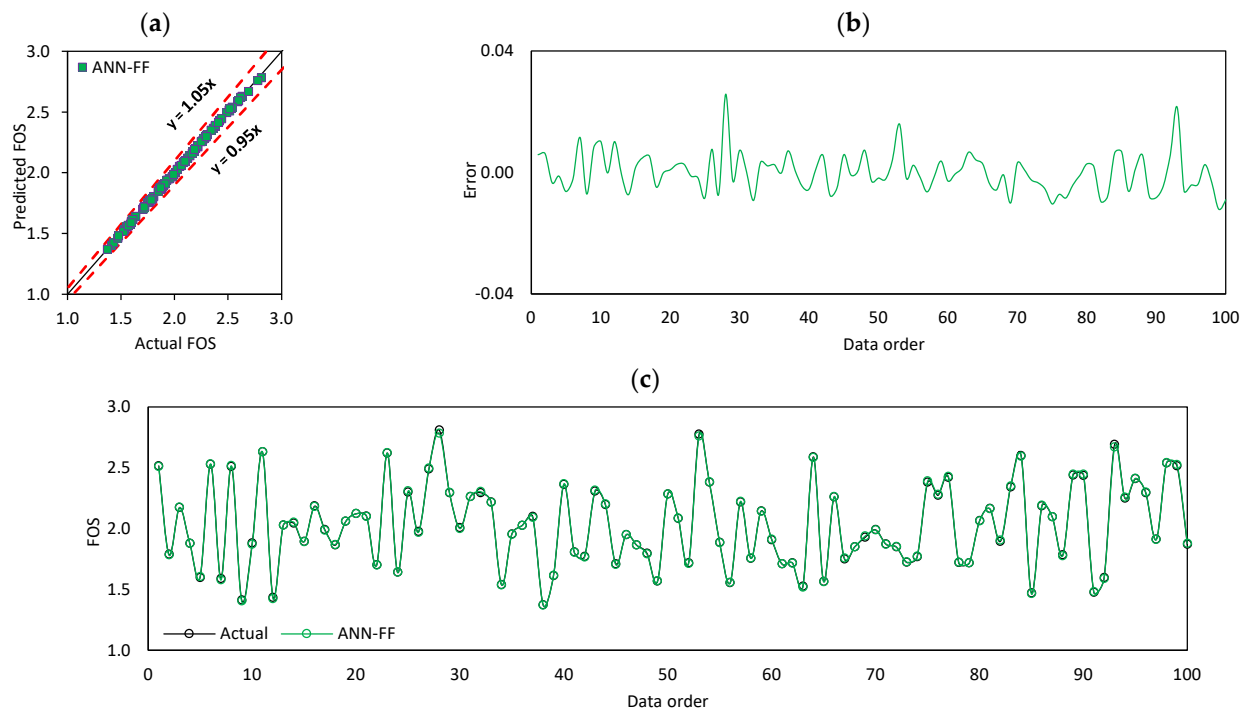


Figure 13. Illustration of (a) scatter plot, (b) error plot, and (c) line plot for the testing dataset.

7.3. Assessment of POF

The results of probabilistic analyses of the volcanic slope of Mount St. Helen are presented in this sub-section. As previously indicated, the ANN-FF model, a superior hybrid ANN, was used to undertake the probabilistic assessments. Assuming a specific mean (μ) for different rock parameters, the standard deviation (σ) was calculated using: $\sigma = \mu \times \text{COV}$. The details of COV considered in this study are presented in Table 4.

Note that the values of COVs considered in this study is in line with the COV range presented in the existing literature. The steps of probabilistic analysis is organized as follows: (i) determination of μ and COVs for different rock parameters viz., c , ϕ , and γ ; (ii) compute the σ_{FOS} of the predicted FOS values; (iii) use rock properties and their standard deviations to produce random values; (iv) select additional input parameters such as k_e ; (v) dataset finalization for five different k_e values; (vi) dataset normalization as per minimum and maximum values of actual database (as presented in Table 1); (vii) estimation of FOS using the developed ANN-FF model, and (viii) the estimation of β and POF as per Section 4.3.

Note that, five different combinations of COV (Cases 1 to 5) were considered in this study. The COVs of c and ϕ were set in the range of 10–30% by 5% and 2–10% by 2%, respectively. However, a constant COV of 5% was considered for parameter γ . Table 4 displays COV values for all five cases. To perform probabilistic analysis, a total of 30 samples were generated against each COV case, resulting in a total of 150 (i.e., 30×5) samples. These samples were investigated against five k_e values. Therefore, 25 instances (i.e., 5 COV cases and 5 k_e sets) were investigated. The results of probabilistic analyses are presented in Table 5. Herein, the values of POF are presented in % terms. According to the results, the values of β exhibit a range of 9.51–14.30, 5.96–9.17, 4.06–6.17, 3.42–5.45, and 2.89–4.64 for COV cases 1 to 5, respectively. Contrarily, the values of β were found to fall within the ranges of 4.64–14.30, 4.23–13.26, 3.63–12.33, 3.44–11.06, and 2.89–9.51 against k_e sets 1 to 5, respectively. In non-seismic conditions, the values of β were determined to be between 4.64 and 14.30, indicating lower POF and a high degree of certainty. For this case, the POF falls in the range of 1.1×10^{-44} to 1.7×10^{-4} . However, in seismic conditions, the values of POF fall between 2.1×10^{-38} and 1.2×10^{-3} against $k_e = 0.05$, 5.5×10^{-33} and 0.01 against $k_e = 0.10$, 9.8×10^{-27} and 0.03 against $k_e = 0.15$, and 9.7×10^{-20} and 0.19 against $k_e = 0.20$. For better illustrations, Figure 14 represents the variation of β and POF for different COV and k_e values.

According to the information presented in Table 5 and Figure 14, β of the Mount St. Helen reduces when COV and k_e increase, indicating higher POF. Also, the impact of COV on the POF was observed throughout a range of k_e values. Thus, it can be stated that the selection of appropriate values for the COVs has a major impact on the slope failure probability. Using GA and MCS, Tun et al. [38] conducted RA of the same slope of the Mount St. Helen. In their studies, the authors assumed material homogeneity and ignored the pore pressure ratio and seismic loading. Using a single COV of 23% for c and 7% for ϕ , Tun et al. [38] reported $\beta = 6.14$ and POF = 0.0%, i.e., very low POF.

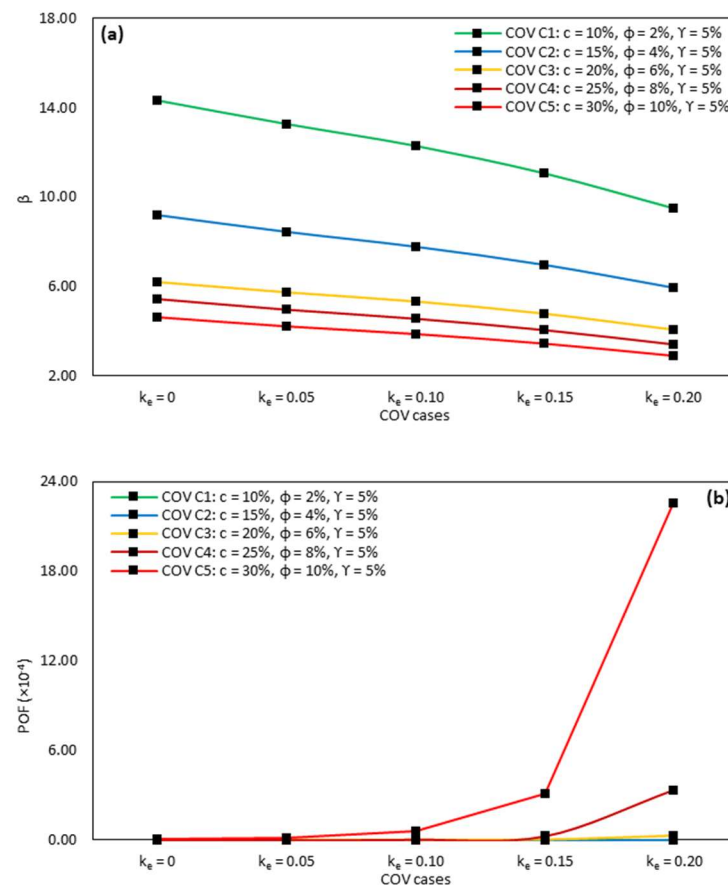
Similarly, using the MCS approach, the β and POF values were reported as 5.89 and 0.0%, respectively. Nonetheless, details of generated samples and a sample calculation for β and POF are presented in Appendix A. Herein, the samples generated with COV Case 1 are only presented. However, the values of β and POF are shown for all the five k_e combinations. The details of weights and biases of the developed ANN-FF model are given in Appendix B, which can be used to assess β and POF for other cases. Moreover, the developed MATLAB model of ANN-FF and DEM profiles are included as Supplementary Materials for future studies.

Table 4. Details of mean and COV cases.

Parameter	Mean	COV (%) Cases					COV Value/Range	Reference
		Case 1	Case 2	Case 3	Case 4	Case 5		
c	1000	10%	15%	20%	25%	30%	23%	Tun et al. [38]
ϕ	40	2%	4%	6%	8%	10%	7%	Tun et al. [38]
γ	24	5%	5%	5%	5%	5%	3–7%	Harr [78]

Table 5. Results of probabilistic analysis.

Cases	β and POF	β and POF (%)				
		Set 1	Set 2	Set 3	Set 4	Set 5
Case 1	β	14.30	13.26	12.33	11.06	9.51
	POF	1.1×10^{-44}	2.1×10^{-38}	5.5×10^{-33}	9.8×10^{-27}	9.7×10^{-20}
Case 2	β	9.17	8.43	7.97	6.97	5.96
	POF	2.4×10^{-18}	1.7×10^{-15}	3.9×10^{-13}	1.6×10^{-10}	1.3×10^{-7}
Case 3	β	6.17	5.72	5.28	4.77	4.06
	POF	3.3×10^{-8}	5.4×10^{-7}	5.4×10^{-6}	9.2×10^{-5}	2.5×10^{-3}
Case 4	β	5.45	4.98	4.67	4.07	3.42
	POF	2.5×10^{-6}	3.2×10^{-5}	2.4×10^{-4}	2.4×10^{-3}	3.1×10^{-2}
Case 5	β	4.64	4.23	3.63	3.44	2.89
	POF	1.7×10^{-4}	1.2×10^{-3}	0.01	0.03	0.19

**Figure 14.** Illustration of (a) β and (b) POF at different COV levels.

8. Summary and Conclusions

RA was carried out on the real topography of Mount St. Helens, which collapsed in 1980 due to an eruption, and the results are described in this study. Initially, the FOS was determined by performing a series of calculations in Scoops3D with various input parameters, such as rock characteristics that vary with location and seismic coefficient. The next step was to construct eight hybrid ANNs, using FOS as an output and the corresponding rock parameters and k_e as inputs. After performance assessment, the best-performing model, i.e., ANN-FF (based on performance in the testing phase with $R^2 = 0.9996$ and $RMSE = 0.0042$), was chosen for probabilistic analyses the Mount St. Helen in seismic and non-seismic scenarios.

For this purpose, five distinct COV combinations were investigated for five different k_e values, varying between 0 and 0.20. According to the experimental results, the POF varies in the range of 1.1×10^{-44} to 1.7×10^{-04} and 2.1×10^{-38} to 0.19 in non-seismic and seismic conditions, respectively. Even at the high COV and seismic levels, the POF was between 9.7×10^{-20} and 0.19. These results indicate that the failure probability of the slope is negligible even at higher COV levels. Thus, it is deduced that if Mount St. Helens does not erupt, COVs will have little effect on the POF. Given the uncertainty of rock properties, the suggested ANN-FF-based RA is determined to be an appropriate solution for calculating the POF of the Mount St. Helen.

Furthermore, the proposed technique demonstrates an accurate estimation of the FOS of the slope irrespective of seismic conditions. The proposed ANN-FF has the following advantages: (i) improved generalization, (ii) faster convergence, and (iii) higher prediction accuracy in both phases. However, the suggested ANN-FF model has higher computational cost than other hybrid ANNs built in this study. In addition, the above investigation was carried out using the upper and lower ranges of rock parameters (as detailed in Table 1). Hence, it can be deduced that the above analysis may not yield satisfactory results beyond these values, which can be considered as one of the limitations of the present study. However, further assessment is required for this case. Therefore, the following points should be considered as the future scope of the study: (i) implementation of improved mechanism to reduce the computational cost of ANN-FF paradigm; (ii) in-depth assessment of slope failure probability at high COV and larger range of c , ϕ , and γ parameters, (iii) adoption of Mononobe-Okabe trick combined with seismic actions for an in-depth assessment, and (iv) a comprehensive assessment of other hybrid models of ANN, RVM, and ELM constructed with different group of OAs. Nevertheless, per the author's knowledge and literature review, this study is the primary implementation of the ANN-FF model to perform probabilistic analyses of the Mount St. Helens in seismic and non-seismic conditions.

Supplementary Materials: The following supporting information can be downloaded at: <https://www.mdpi.com/article/10.3390/math11183809/s1>, The developed MATLAB model and Scoops3D DEM profiles are attached as Supplementary Materials.

Author Contributions: Conceptualization, A.B. (Avijit Burman) and A.B. (Abidhan Bardhan); methodology, S.K. and A.B. (Avijit Burman); software, S.K. and A.B. (Abidhan Bardhan); formal analysis, S.K. and A.B. (Abidhan Bardhan); validation, S.K. and A.B. (Abidhan Bardhan); writing—original draft preparation, S.K., S.S.C., A.B. (Avijit Burman), R.K.S. and A.B. (Abidhan Bardhan); writing—review and editing, A.B. (Abidhan Bardhan) and P.G.A. All authors have read and agreed to the published version of the manuscript.

Funding: This research received no external funding.

Data Availability Statement: Attached as Supplementary Materials.

Conflicts of Interest: The authors declare no conflict of interest.

Abbreviations

2D	Two-dimensional
3D	Three-dimensional
ABC	Artificial bee colony
ALO	Ant lion optimizer
ANN	Artificial neural network
ANN-ABC	Hybrid model of ANN and ABC
ANN-ALO	Hybrid model of ANN and ALO
ANN-BBO	Hybrid model of ANN and BBO
ANN-CPA	Hybrid model of ANN and CPA
ANN-DE	Hybrid model of ANN and DE
ANN-EO	Hybrid model of ANN and EO

ANN-FF	Hybrid model of ANN and FF
ANN-GA	Hybrid model of ANN and GA
ANN-PSO	Hybrid model of ANN and PSO
BBBC	Big Bang Big Crunch
BBO	Biogeography based optimization
COV	Coefficient of variation
CPA	Colony predation algorithm
DE	Differential evolution
DEM	Digital elevation model
EA	Evolutionary algorithms
ELM	Extreme learning machine
EO	Equilibrium optimizer
ES	Evolution strategy
FDO	Fitness Dependent Optimizer
FF	Fire fly algorithm
FORM	First-order reliability method
FOS	Factor of safety
FOSM	First-order second-moment method
GA	Genetic algorithm
GIS	Geographic information system
GSA	Gravitational search algorithm
GWO	Grey wolf optimizer
HS	Harmony search
ICA	Imperialist competitive algorithm
LEM	Limit equilibrium method
MAE	Mean absolute error
MARS	Multivariate adaptive regression splines
MCS	Monte Carlo simulation
ML	Machine learning
NSE	Nash-Sutcliffe efficiency
OA	Optimization algorithm
PI	Performance index
POF	Probability of failure
PSO	Particle swarm optimization
R ²	Coefficient of determination
RA	Reliability analysis
RMSE	Root mean square error
RSM	Response surface method
RVM	Relevance vector machine
SA	Simulated annealing
SI	Swarm intelligence
SRM	Strength reduction method
SSA	Salp swarm algorithm
TLBO	Teaching learning-based optimization
USGS	United States Geological Survey
WMAPE	Weighted mean absolute percentage error

Nomenclature

c	Cohesion
itr_{max}	maximum number of iterations
k_e	seismic coefficient
lb	Lower bound
N_{HL}	Number of hidden layers
N_H	Number of hidden neurons
N_S	Population/swarm size
ub	Upper bound

ϕ	Angle of internal friction
γ	Bulk density
β	Reliability index
μ	Mean
σ	Standard deviation
μ_{FOS}	Mean of FOS
σ_{FOS}	Standard deviation of FOS

Appendix A. Sample Calculation

Details of generated samples and estimation of β and POF are presented in Table A1.

Table A1. Generated parameters and estimated FOS for COV Case 1.

c	ϕ	γ	FOS at $k_e = 0$	FOS at $k_e = 0.05$	FOS at $k_e = 0.10$	FOS at $k_e = 0.15$	FOS at $k_e = 0.20$
1046.41	41.15	23.62	2.314	2.089	1.897	1.734	1.587
797.24	41.58	24.32	2.164	1.950	1.771	1.619	1.483
1049.63	40.14	23.84	2.248	2.030	1.846	1.687	1.542
1148.52	39.24	22.88	2.283	2.060	1.872	1.708	1.560
885.52	39.70	21.71	2.175	1.959	1.777	1.623	1.485
921.36	40.39	23.78	2.182	1.969	1.789	1.636	1.498
1038.03	40.56	23.88	2.265	2.045	1.859	1.699	1.554
940.10	38.51	25.82	2.034	1.842	1.682	1.540	1.407
1033.03	39.00	25.70	2.119	1.918	1.748	1.599	1.460
878.54	39.22	26.09	2.032	1.840	1.680	1.539	1.408
852.49	39.70	23.77	2.100	1.895	1.723	1.575	1.441
902.73	40.02	22.54	2.182	1.966	1.784	1.630	1.492
1015.86	41.65	22.80	2.347	2.118	1.922	1.757	1.609
998.84	40.78	22.61	2.288	2.064	1.873	1.712	1.567
942.17	39.21	25.13	2.091	1.891	1.724	1.577	1.443
977.59	39.21	24.06	2.141	1.934	1.760	1.610	1.472
1149.28	39.61	23.85	2.278	2.057	1.869	1.706	1.557
1170.86	39.69	25.78	2.237	2.021	1.838	1.676	1.527
865.25	40.80	22.80	2.197	1.979	1.795	1.640	1.501
1088.80	40.22	23.02	2.301	2.077	1.887	1.723	1.575
933.46	40.11	22.94	2.195	1.979	1.798	1.643	1.504
1064.66	40.38	24.35	2.258	2.040	1.855	1.695	1.549
932.30	38.96	24.87	2.078	1.879	1.712	1.567	1.433
1111.25	39.74	26.13	2.195	1.986	1.808	1.651	1.507
1010.37	39.19	25.14	2.131	1.928	1.756	1.606	1.468
1075.73	40.25	23.85	2.271	2.051	1.864	1.703	1.557
1112.64	40.15	24.03	2.283	2.062	1.874	1.711	1.563
998.55	41.15	25.07	2.242	2.026	1.843	1.686	1.543
921.31	40.47	22.52	2.221	2.001	1.816	1.659	1.519
1137.51	39.23	23.13	2.269	2.048	1.861	1.699	1.551
μ_{FOS}			2.204	1.990	1.809	1.654	1.512
σ_{FOS}			0.0842	0.0747	0.0659	0.0591	0.0539
β			14.30	13.26	12.28	11.06	9.51
POF (%)			1.1×10^{-44}	2.1×10^{-38}	5.5×10^{-33}	9.8×10^{-27}	9.7×10^{-20}

Appendix B. Details of Weights and Biases

Details of weights and biases for the developed ANN-FF model are presented below. Input-hidden layer weights:

1.2128	1.1998	−0.0983	0.0943	0.4363	−0.3550	−0.4031	−0.8791
1.7655	0.0843	−0.4341	0.2536	2.1245	−0.0737	1.6471	−2.0288
−0.3319	1.1062	0.0289	−0.0084	0.4660	−0.6024	1.3598	0.4425
0.9995	0.7243	0.4918	−0.2207	0.1650	−0.9283	0.2813	−1.2230]

Hidden layer biases:

[−2.2941	−1.3986	1.4235	0.0455	0.2659	−0.8758	−1.8870	2.4074]
----------	---------	--------	--------	--------	---------	---------	---------

Hidden-output layer weights:

[−0.0643	−0.0304	−1.1639	1.3973	0.0009	0.0614	0.0022	−0.0685]
----------	---------	---------	--------	--------	--------	--------	----------

Output layer bias:

[0.7887]

References

1. Siebert, L. Large volcanic debris avalanches: Characteristics of source areas, deposits, and associated eruptions. *J. Volcanol. Geotherm. Res.* **1984**, *22*, 163–197. [\[CrossRef\]](#)
2. Ui, T. Volcanic dry avalanche deposits—Identification and comparison with nonvolcanic debris stream deposits. *J. Volcanol. Geotherm. Res.* **1983**, *18*, 135–150. [\[CrossRef\]](#)
3. Voight, B.; Elsworth, D. Failure of volcano slopes. *Geotechnique* **1997**, *47*, 1–31. [\[CrossRef\]](#)
4. Voight, B.; Janda, R.J.; Glicken, H.; Douglass, P.M. Nature and mechanics of the Mount St Helens rockslide-avalanche of 18 May 1980. *Geotechnique* **1983**, *33*, 243–273. [\[CrossRef\]](#)
5. Siebert, L.; Glicken, H.; Ui, T. Volcanic hazards from Bezymianny-and Bandai-type eruptions. *Bull. Volcanol.* **1987**, *49*, 435–459. [\[CrossRef\]](#)
6. Reid, M.E. Transient thermal pressurization in hydrothermal systems: A cause of large-scale edifice collapse at volcanoes? *Geol. Soc. Am. Abstr. Programs* **1994**, *26*, A376.
7. Bishop, A.W. The use of the slip circle in the stability analysis of slopes. *Geotechnique* **1955**, *5*, 7–17. [\[CrossRef\]](#)
8. Zhang, Y.; Chen, G.; Zheng, L.; Li, Y.; Zhuang, X. Effects of geometries on three-dimensional slope stability. *Can. Geotech. J.* **2013**, *50*, 233–249. [\[CrossRef\]](#)
9. Kalatehjari, R.; Arefnia, A.; Rashid, A.S.A.; Ali, N.; Hajihassani, M. Determination of Three-Dimensional Shape of Failure in Soil Slopes. *Can. Geotech. J.* **2015**, *52*, 1283–1301. [\[CrossRef\]](#)
10. Hovland, H.J. Three-dimensional slope stability analysis method. *J. Geotech. Eng. Div.* **1977**, *103*, 971–986. [\[CrossRef\]](#)
11. Xing, Z. Three-dimensional stability analysis of concave slopes in plan view. *J. Geotech. Eng.* **1988**, *114*, 658–671. [\[CrossRef\]](#)
12. Sun, C.; Chai, J.; Xu, Z.; Qin, Y. 3D stability charts for convex and concave slopes in plan view with homogeneous soil based on the strength-reduction method. *Int. J. Geomech.* **2017**, *17*, 6016034. [\[CrossRef\]](#)
13. Kumar, S.; Choudhary, S.S.; Burman, A. Recent advances in 3D slope stability analysis: A detailed review. *Model. Earth Syst. Environ.* **2022**, *9*, 1445–1462. [\[CrossRef\]](#)
14. Hungr, O. An extension of Bishop's simplified method of slope stability analysis to three dimensions. *Geotechnique* **1987**, *37*, 113–117. [\[CrossRef\]](#)
15. Bishop, A.W. The analysis of stability of slopes. *Géotechnique* **1955**, *5*, 7. [\[CrossRef\]](#)
16. Lam, L.; Fredlund, D. A general limit equilibrium model for three-dimensional slope stability analysis. *Can. Geotech. J.* **1993**, *30*, 905–919. [\[CrossRef\]](#)
17. Fredlund, D.G.; Krahn, J. Comparison of slope stability methods of analysis. *Can. Geotech. J.* **1977**, *14*, 429–439. [\[CrossRef\]](#)
18. An, Y.; Li, J.; Yue, J.; Zhou, J. Effect of seepage force on tunnel face stability using limit analysis with SRM. *Geotech. Geol. Eng.* **2021**, *39*, 1743–1751. [\[CrossRef\]](#)
19. Liu, S.Y.; Shao, L.T.; Li, H.J. Slope stability analysis using the limit equilibrium method and two finite element methods. *Comput. Geotech.* **2015**, *63*, 291–298. [\[CrossRef\]](#)
20. Zhao, H. Slope reliability analysis using a support vector machine. *Comput. Geotech.* **2008**, *35*, 459–467. [\[CrossRef\]](#)
21. Safa, M.; Maleka, A.; Arjomand, M.A.; Khorami, M.; Shariati, M. Strain rate effects on soil-geosynthetic interaction in fine-grained soil. *Geomech. Eng.* **2019**, *19*, 533.
22. Duncan, J.M. Factors of safety and reliability in geotechnical engineering. *J. Geotech. Geoenviron. Eng.* **2000**, *126*, 307–316. [\[CrossRef\]](#)
23. Cao, Z.; Wang, Y.; Li, D. *Probabilistic Approaches for Geotechnical Site Characterization and Slope Stability Analysis*; Springer: Berlin/Heidelberg, Germany, 2017.
24. Phoon, K.-K.; Ching, J. *Risk and Reliability in Geotechnical Engineering*; CRC Press: Boca Raton, FL, USA, 2015.
25. Xie, M.; Esaki, T.; Zhou, G.; Mitani, Y. Three-dimensional stability evaluation of landslides and a sliding process simulation using a new geographic information systems component. *Environ. Geol.* **2003**, *43*, 503–512. [\[CrossRef\]](#)
26. Wong, F.S. Slope reliability and response surface method. *J. Geotech. Eng.* **1985**, *111*, 32–53. [\[CrossRef\]](#)
27. Zhao, H.; Yin, S.; Ru, Z. Relevance vector machine applied to slope stability analysis. *Int. J. Numer. Anal. Methods Géoméch.* **2012**, *36*, 643–652. [\[CrossRef\]](#)
28. Bardhan, A.; Samui, P. Probabilistic slope stability analysis of Heavy-haul freight corridor using a hybrid machine learning paradigm. *Transp. Geotech.* **2022**, *37*, 100815. [\[CrossRef\]](#)

29. Deng, J. Structural reliability analysis for implicit performance function using radial basis function network. *Int. J. Solids Struct.* **2006**, *43*, 3255–3291. [\[CrossRef\]](#)
30. Deng, J.; Gu, D.; Li, X.; Yue, Z.Q. Structural reliability analysis for implicit performance functions using artificial neural network. *Struct. Saf.* **2005**, *27*, 25–48. [\[CrossRef\]](#)
31. Cho, S.E. Probabilistic stability analyses of slopes using the ANN-based response surface. *Comput. Geotech.* **2009**, *36*, 787–797. [\[CrossRef\]](#)
32. Erzin, Y.; Cetin, T. The use of neural networks for the prediction of the critical factor of safety of an artificial slope subjected to earthquake forces. *Sci. Iran.* **2012**, *19*, 188–194. [\[CrossRef\]](#)
33. Kang, F.; Xu, Q.; Li, J. Slope reliability analysis using surrogate models via new support vector machines with swarm intelligence. *Appl. Math. Model.* **2016**, *40*, 6105–6120. [\[CrossRef\]](#)
34. Li, S.; Zhao, H.; Ru, Z. Relevance vector machine-based response surface for slope reliability analysis. *Int. J. Numer. Anal. Methods Géoméch.* **2017**, *41*, 1332–1346. [\[CrossRef\]](#)
35. Chen, J.; Wen, L.; Bi, C.; Liu, Z.; Liu, X.; Yin, L.; Zheng, W. Multifractal analysis of temporal and spatial characteristics of earthquakes in Eurasian seismic belt. *Open Geosci.* **2023**, *15*, 20220482. [\[CrossRef\]](#)
36. Reid, M.E.; Christian, S.B.; Brien, D.L.; Henderson, S. Scoops3D—Software to analyze three-dimensional slope stability throughout a digital landscape. In *U.S. Geological Survey Techniques and Methods*; U.S. Geological Survey: Reston, VA, USA, 2015.
37. Le, L.T.; Nguyen, H.; Dou, J.; Zhou, J. A comparative study of PSO-ANN, GA-ANN, ICA-ANN, and ABC-ANN in estimating the heating load of buildings' energy efficiency for smart city planning. *Appl. Sci.* **2019**, *9*, 2630. [\[CrossRef\]](#)
38. Tun, Y.W.; Llano-Serna, M.A.; Pedroso, D.M.; Scheuermann, A. Multimodal reliability analysis of 3D slopes with a genetic algorithm. *Acta Geotech.* **2019**, *14*, 207–223. [\[CrossRef\]](#)
39. Glicken, H. *Rockslide-Debris Avalanche of May 18, 1980, Mount St. Helens Volcano, Washington*; U.S. Geological Survey, Cascades Volcano Observatory: Reston, VA, USA, 1996.
40. Hopson, C.A.; Melson, W.G. Stratigraphy of Mount St. Helens 1980 crater walls. *EOS. Trans. Am. Geophys. Union* **1982**, *63*, 13.
41. Balasubramanian, A. *Digital Elevation Model (DEM) in GIS*; University of Mysore: Mysuru, India, 2017.
42. Xu, Y.; Zhao, M.-W.; Lu, J.; Wang, C.; Jiang, L.; Yang, C.-C.; Huang, X.-L. Methods for the construction of DEMs of artificial slopes considering morphological features and semantic information. *J. Mt. Sci.* **2022**, *19*, 563–577. [\[CrossRef\]](#)
43. Wise, S. Assessing the quality for hydrological applications of digital elevation models derived from contours. *Hydrol. Process.* **2000**, *14*, 1909–1929. [\[CrossRef\]](#)
44. Zhou, G.; Zhou, X.; Song, Y.; Xie, D.; Wang, L.; Yan, G.; Hu, M.; Liu, B.; Shang, W.; Gong, C.; et al. Design of supercontinuum laser hyperspectral light detection and ranging (LiDAR)(SCLaHS LiDAR). *Int. J. Remote Sens.* **2021**, *42*, 3731–3755. [\[CrossRef\]](#)
45. Zhou, G.; Li, W.; Zhou, X.; Tan, Y.; Lin, G.; Li, X.; Deng, R. An innovative echo detection system with STM32 gated and PMT adjustable gain for airborne LiDAR. *Int. J. Remote Sens.* **2021**, *42*, 9187–9211. [\[CrossRef\]](#)
46. Zhou, G.; Deng, R.; Zhou, X.; Long, S.; Li, W.; Lin, G.; Li, X. Gaussian inflection point selection for LiDAR hidden echo signal decomposition. *IEEE Geosci. Remote Sens. Lett.* **2021**, *19*, 1–5. [\[CrossRef\]](#)
47. Zhou, G.; Yang, Z. Analysis for 3-D morphology structural changes for underwater topographical in Culebrita Island. *Int. J. Remote Sens.* **2023**, *44*, 2458–2479. [\[CrossRef\]](#)
48. Zhuo, Z.; Du, L.; Lu, X.; Chen, J.; Cao, Z. Smoothed Lv distribution based three-dimensional imaging for spinning space debris. *IEEE Trans. Geosci. Remote Sens.* **2022**, *60*, 1–13. [\[CrossRef\]](#)
49. Liu, Z.; Xu, J.; Liu, M.; Yin, Z.; Liu, X.; Yin, L.; Zheng, W. Remote sensing and geostatistics in urban water-resource monitoring: A review. *Mar. Freshw. Res.* **2023**, *74*, 747–765. [\[CrossRef\]](#)
50. Cavazzi, S.; Corstanje, R.; Mayr, T.; Hannam, J.; Fealy, R. Are fine resolution digital elevation models always the best choice in digital soil mapping? *Geoderma* **2013**, *195*, 111–121. [\[CrossRef\]](#)
51. Golafshani, E.M.; Behnood, A.; Arashpour, M. Predicting the compressive strength of normal and High-Performance Concretes using ANN and ANFIS hybridized with Grey Wolf Optimizer. *Constr. Build. Mater.* **2020**, *232*, 117266. [\[CrossRef\]](#)
52. Apostolopoulou, M.; Asteris, P.G.; Armaghani, D.J.; Douvika, M.G.; Lourenço, P.B.; Cavaleri, L.; Bakolas, A.; Moropoulou, A. Mapping and holistic design of natural hydraulic lime mortars. *Cem. Concr. Res.* **2020**, *136*, 106167. [\[CrossRef\]](#)
53. Asteris, P.G.; Kokoris, S.; Gavriilaki, E.; Tsoukalas, M.Z.; Houpas, P.; Paneta, M.; Koutzas, A.; Argyropoulos, T.; Alkayem, N.F.; Armaghani, D.J.; et al. Early prediction of COVID-19 outcome using artificial intelligence techniques and only five laboratory indices. *Clin. Immunol.* **2023**, *246*, 109218. [\[CrossRef\]](#)
54. Asteris, P.G.; Gavriilaki, E.; Touloumenidou, T.; Koravou, E.; Koutra, M.; Papayanni, P.G.; Pouleres, A.; Karali, V.; Lemonis, M.E.; Mamou, A.; et al. Genetic prediction of icu hospitalization and mortality in COVID-19 patients using artificial neural networks. *J. Cell. Mol. Med.* **2022**, *26*, 1445–1455. [\[CrossRef\]](#)
55. Asteris, P.G.; Armaghani, D.J.; Hatzigeorgiou, G.D.; Karayannis, C.G.; Pilakoutas, K. Predicting the shear strength of reinforced concrete beams using Artificial Neural Networks. *Comput. Concr. An. Int. J.* **2019**, *24*, 469–488.
56. Elaziz, M.A.; Dahou, A.; Abualigah, L.; Yu, L.; Alshinwan, M.; Khasawneh, A.M.; Lu, S. Advanced metaheuristic optimization techniques in applications of deep neural networks: A review. *Neural Comput. Appl.* **2021**, *33*, 14079–14099. [\[CrossRef\]](#)
57. Seyedali, M. The ant lion optimizer. *Adv. Eng. Softw.* **2015**, *83*, 80–98.
58. Tu, J.; Chen, H.; Wang, M.; Gandomi, A.H. The colony predation algorithm. *J. Bionic Eng.* **2021**, *18*, 674–710. [\[CrossRef\]](#)
59. Yang, X.S.; He, X. Firefly algorithm: Recent advances and applications. *Int. J. Swarm Intell.* **2013**, *1*, 36–50. [\[CrossRef\]](#)

60. Mirjalili, S.; Mirjalili, S.M.; Lewis, A. Grey Wolf Optimizer. *Adv. Eng. Softw.* **2014**, *69*, 46–61. [\[CrossRef\]](#)
61. Kennedy, J.; Eberhart, R. Particle swarm optimization. In Proceedings of the ICNN'95—International Conference on Neural Networks, Perth, WA, Australia, 27 November 1995–1 December 1995; IEEE: Piscataway, NJ, USA, 1995; Volume 4, pp. 1942–1948.
62. Abualigah, L.; Shehab, M.; Alshinwan, M.; Alabool, H. Salp swarm algorithm: A comprehensive survey. *Neural Comput. Appl.* **2020**, *32*, 11195–11215. [\[CrossRef\]](#)
63. Abdullah, J.M.; Ahmed, T. Fitness dependent optimizer: Inspired by the bee swarming reproductive process. *IEEE Access* **2019**, *7*, 43473–43486. [\[CrossRef\]](#)
64. Geem, Z.W.; Kim, J.H.; Loganathan, G.V. A new heuristic optimization algorithm: Harmony search. *Simulation* **2001**, *76*, 60–68. [\[CrossRef\]](#)
65. Atashpaz-Gargari, E.; Lucas, C. Imperialist competitive algorithm: An algorithm for optimization inspired by imperialistic competition. In Proceedings of the 2007 IEEE Congress on Evolutionary Computation, Singapore, 25–28 September 2007; IEEE: Piscataway, NJ, USA, 2007; pp. 4661–4667.
66. Rao, R.V.; Savsani, V.J.; Vakharia, D.P. Teaching–learning–based optimization: A novel method for constrained mechanical design optimization problems. *Comput. Aided Des.* **2011**, *43*, 303–315. [\[CrossRef\]](#)
67. Simon, D. Biogeography-based optimization. *IEEE Trans. Evol. Comput.* **2008**, *12*, 702–713. [\[CrossRef\]](#)
68. Storn, R.; Price, K. Differential evolution—a simple and efficient heuristic for global optimization over continuous spaces. *J. Glob. Optim.* **1997**, *11*, 341. [\[CrossRef\]](#)
69. Rechenberg, I. Evolution strategy: Nature's way of optimization. In *Optimization: Methods and Applications, Possibilities and Limitations: Proceedings of an International Seminar Organized by Deutsche Forschungsanstalt für Luft-und Raumfahrt (DLR), Bonn, June*; Springer: Berlin/Heidelberg, Germany, 1989; pp. 106–126.
70. Goldberg, D.E.; Holland, J.H. Genetic Algorithms and Machine Learning. *Mach. Learn.* **1988**, *3*, 95–99. [\[CrossRef\]](#)
71. Erol, O.K.; Eksin, I. A new optimization method: Big bang–big crunch. *Adv. Eng. Softw.* **2006**, *37*, 106–111. [\[CrossRef\]](#)
72. Faramarzi, A.; Heidarinejad, M.; Stephens, B.; Mirjalili, S. Equilibrium optimizer: A novel optimization algorithm. *Knowl.-Based Syst.* **2020**, *191*, 105190. [\[CrossRef\]](#)
73. Rashedi, E.; Nezamabadi-Pour, H.; Saryazdi, S. GSA: A gravitational search algorithm. *Inf. Sci.* **2009**, *179*, 2232–2248. [\[CrossRef\]](#)
74. Kirkpatrick, S. Optimization by simulated annealing: Quantitative studies. *J. Stat. Phys.* **1984**, *34*, 975–986. [\[CrossRef\]](#)
75. Koopialipoor, M.; Fallah, A.; Armaghani, D.J.; Azizi, A.; Mohamad, E.T. Three hybrid intelligent models in estimating flyrock distance resulting from blasting. *Eng. Comput.* **2019**, *35*, 243–256. [\[CrossRef\]](#)
76. Chen, D.; Wang, Q.; Li, Y.; Li, Y.; Zhou, H.; Fan, Y. A general linear free energy relationship for predicting partition coefficients of neutral organic compounds. *Chemosphere* **2020**, *247*, 125869. [\[CrossRef\]](#)
77. Wu, Z.; Huang, B.; Fan, J.; Chen, H. Homotopy based stochastic finite element model updating with correlated static measurement data. *Measurement* **2023**, *210*, 112512. [\[CrossRef\]](#)
78. Harr, M.E. *The Civil Engineering Handbook*; CRC Press: Boca Raton, FL, USA, 2002; Chapter 18.

Disclaimer/Publisher's Note: The statements, opinions and data contained in all publications are solely those of the individual author(s) and contributor(s) and not of MDPI and/or the editor(s). MDPI and/or the editor(s) disclaim responsibility for any injury to people or property resulting from any ideas, methods, instructions or products referred to in the content.